Small

NANO · MICRO small
www.small-journal.com

RESEARCH ARTICLE

How Slippery Surfaces Retain Their Function: Lubricant Film Dynamics Upon Droplet Contact

Shivam Gupta[1] | Bidisha Bhatt[1] | Zhaohe Dai[2] | Krishnacharya Khare[1]

[1]Department of Physics, Indian Institute of Technology Kanpur, Kanpur, Uttar Pradesh, India | [2]Department of Mechanics and Engineering Science, State Key Laboratory for Turbulence and Complex Systems, College of Engineering, Peking University, Beijing, China

Correspondence: Zhaohe Dai (daizh@pku.edu.cn) | Krishnacharya Khare (kcharya@iitk.ac.in)

Received: 2 February 2026 | **Revised:** 30 April 2026 | **Accepted:** 12 May 2026

Keywords: capillarity | DW-RICM | liquid bridges | slippery lubricated surfaces | surface evolver | thin-film dynamics

ABSTRACT

Slippery surfaces, prepared by coating functionalized solids with thin viscous lubricant films, offer excellent liquid repellency and are promising for applications ranging from water harvesting to anti-biofouling. Upon liquid contact, the lubricant film deforms, critically influencing phenomena such as droplet coalescence, mobility, and lubricant depletion, yet its dynamics remain unclear. In this study, using principles of fluid dynamics, optics, and capillarity, the spatio-temporal evolution of lubricant films on smooth solid surfaces upon contact with sessile liquids is presented, and their equilibrium configurations are numerically determined. It is found that beneath sessile liquids, the lubricant films exhibit three distinct dynamic stages, while beyond liquids, their maxima propagate according to a defined scaling law. By controlling the key system parameters, partial lift-off of liquid bridges is also demonstrated, a previously unreported phenomenon driven by a capillary rise-like mechanism. Finally, the equilibrium configuration is revealed in which the film thickness at the droplet center stabilizes at tens of nanometers, independent of the initial film thickness. These findings provide fundamental insights into the coupled wetting and transport processes that govern the stability and performance of lubricant-infused slippery surfaces.

1 | Introduction

From various natural to industrial processes, it is often required to have a low adhesion of liquids to surfaces. Typically, superhydrophobic surfaces (SHSs), inspired by lotus leaves, are utilized to achieve such requirements. However, SHSs have significant limitations, which arise due to the direct contact between liquids and solid surfaces, and the replacement of air pockets under unfavorable conditions [1–11]. A key advancement came from studying *Nepenthes* pitcher plants, which use a combination of nectar and water to make insects lose their grip and become their prey [12, 13]. This mechanism led to the idea of coating surfaces with thin lubricant films to prevent the direct contact between the liquids and the underlying substrates. When these lubricant films are stable, liquid droplets move easily across lubricated surfaces, a characteristic often described as "slippery". Slippery surfaces have shown potential in a wide range of applications, such as self-healing, anti-icing, water harvesting, enhanced heat transfer, and anti-biofouling. These surfaces even outperform SHSs in many of these applications [14–20].

When a liquid droplet contacts a slippery surface, unbalanced forces at the three-phase contact line draw the lubricant upward, forming a negative Laplace pressure region known as the wetting ridge. The pressure difference drives the lubricant flow toward the ridge from both beneath and beyond the droplet, resulting in a time-dependent evolution of the lubricant morphology. Studies have demonstrated that thicker films beneath liquid and larger wetting ridges enhance droplet mobility and coalescence, respectively, whereas smaller ridges are more effective in reducing

lubricant depletion [9, 21–27]. To understand such phenomena, it is necessary to elucidate the lubricant dynamics both beneath and beyond a sessile liquid droplet.

Recently, Dai and Vella theoretically examined the film dynamics upon contact of a non-evaporating sessile droplet [28]. Using a simplified two-dimensional model with equal interfacial tensions, they captured the essential features of film evolution, primarily focusing on the slow dynamics of the wetting ridge. While this framework provided valuable physical insights, it cannot be applied directly to experimental systems, which are typically axisymmetric and involve unequal interfacial tensions. On the experimental side, progress remained limited due to several challenges, including the difficulty in observing thin films due to poor refractive index contrast, unstable lubricant films, and moving contact lines caused by droplet evaporation and mobility. A significant advance in observing stable silicone oil films beneath aqueous droplets was achieved by Daniel et al. [29]. Using dual-wavelength reflection interference contrast microscopy (DW-RICM), they found that thin films exhibit a dimple-shaped profile, with the minimum thickness occurring at the inner edge of the droplet. However, evaporation and mobility of aqueous droplets still limited a detailed understanding of the film dynamics.

In this work, we address these gaps by employing an unconventional, non-evaporating system with high refractive index contrast. By combining this with an extended theoretical model for axisymmetric geometries along with unequal interfacial tensions, we provide detailed insights into three-stage film dynamics and the phenomenon of partial liquid lift-off. To our knowledge, these dynamical stages and the lift-off transition have not been previously reported for such slippery systems. Also, since the experimental system considered here satisfies the fundamental criteria for a slippery system, the experimental and numerical results presented in this study can be generalized and applied to any slippery system to further investigate the multi-functionality and longevity of slippery surfaces.

2 | Results

2.1 | Dynamics Beneath Sessile Liquids

We begin by addressing the aforementioned experimental challenges. We addressed the challenges of liquid evaporation and poor refractive index contrast by using an unconventional system of Krytox (a perfluorinated oil), silicone oil, and glass as the top liquid, lubricant, and solid, respectively, and imaged the system with a confocal microscope. To unambiguously resolve film thickness, the microscope was configured with two lasers ($\lambda_1 = 488$ nm and $\lambda_2 = 638$ nm) and two separate detectors, operating in a dual-channel mode (Experimental Section and Sections S3 and S4). To ensure that the system satisfied the lubricant stability criteria, the glass surfaces were chemically modified with polymer brushes (Experimental Section and Sections S5 and S6) [21, 29, 30]. The unintended droplet motion was prevented by holding its one end using a needle (inset 2 of Figure 1). It was found that for the complete immobilization of Krytox, the needle size should be comparable to the radius of the three-phase contact line. We thus study the thin-film dynamics upon contact with positive Laplace pressure liquid bridges (hereinafter referred to as liquid bridges) and theoretically provide insights into the dynamics for the case of sessile droplets.

Due to the low contact angle of Krytox on silicone oil ($\approx 40°$), Krytox, held at one end by a needle, contacts the surface with a negative Laplace pressure. Thus, subsequent to contact, the needle was retracted to a set height, forming a positive Laplace pressure liquid bridge (Experimental Section and Sections S7 and S8). For all experiments, the needle was positioned far from the Krytox-oil interface; thus, it does not physically obstruct the lubricant dynamics.

To simultaneously determine the Laplace pressure of liquid bridges and the profile of thin films, the system was visualized from the side and bottom. Figure 1 shows the employed experimental setup along with a typical side and bottom view of the system, captured 1 min after Krytox, held by a needle, contacted a silicone oil-coated glass surface (initial film thickness $h_0 = 5.9\,\mu$m). We define the endpoints of the wetting ridge, located beneath and beyond the liquid, as the edge and neck, respectively, and the first local maxima of the film beyond the liquid as the bump (Figure 1b).

Next, we experimentally determined the spatial evolution of the thin film beneath liquid bridges over time scales ranging from tens of seconds to tens of minutes (Movies S1 and S2). Figure 2 displays the interferometry images, along with the corresponding film profiles shown in the bottom panels for two different initial thicknesses, $h_{0,1} = 1.5\,\mu$m and $h_{0,2} = 5.9\,\mu$m, with similar values of contact line radius r_c and Laplace pressure of liquid bridge ΔP_{liq}. For the case of $h_{0,1}$, the thin film initially at $t = 20$ s exhibited a wimple (characterized by a central minimum, followed by maxima, and then another minima), which gradually transitioned into a dimple (characterized by a central maximum followed by minima) within about 4 min. During this transition, the height at the center increased to about 2.1 μm, exceeding the initial thickness $h_{0,1}$. The transition behavior from wimple to dimple is similar to the thin-film dynamics when liquids within an external ambient liquid are pushed from very close to a wall [31]. As time progressed, the lubricant continued to drain beneath the liquid bridge while retaining the dimple profile. For the case of $h_{0,2}$, we observed a slightly different behavior compared to the case of $h_{0,1}$. Initially, the wimple did not appear; instead, the thin-film dynamics began with a dimple profile ($t = 1$ min, Figure 2b) and retained this shape during most of the observation period. This behavior is similar to that reported by Daniel et al. [29]. The beneath lubricant film also exhibited a significantly faster drainage rate compared to $h_{0,1}$. During the drainage process, the edge continued to propagate toward the center and, remarkably, merged after about 58 min. Subsequently, the liquid bridge partially lifted off from the slippery surface (mediated by the lubricant), and the height at the center began to increase. Notably, this increase occurred at a significantly faster rate, with height at the center reaching about 800 nm within just 4 minutes of merging. Although moving droplets have been observed to oleoplan on slippery surfaces [29], to our knowledge, the partial lift-off (hereinafter referred to as lift-off) behavior of sessile liquids on slippery surfaces has not been reported previously. To further investigate the lift-off phenomenon, we conducted an additional set of experiments for similar values of

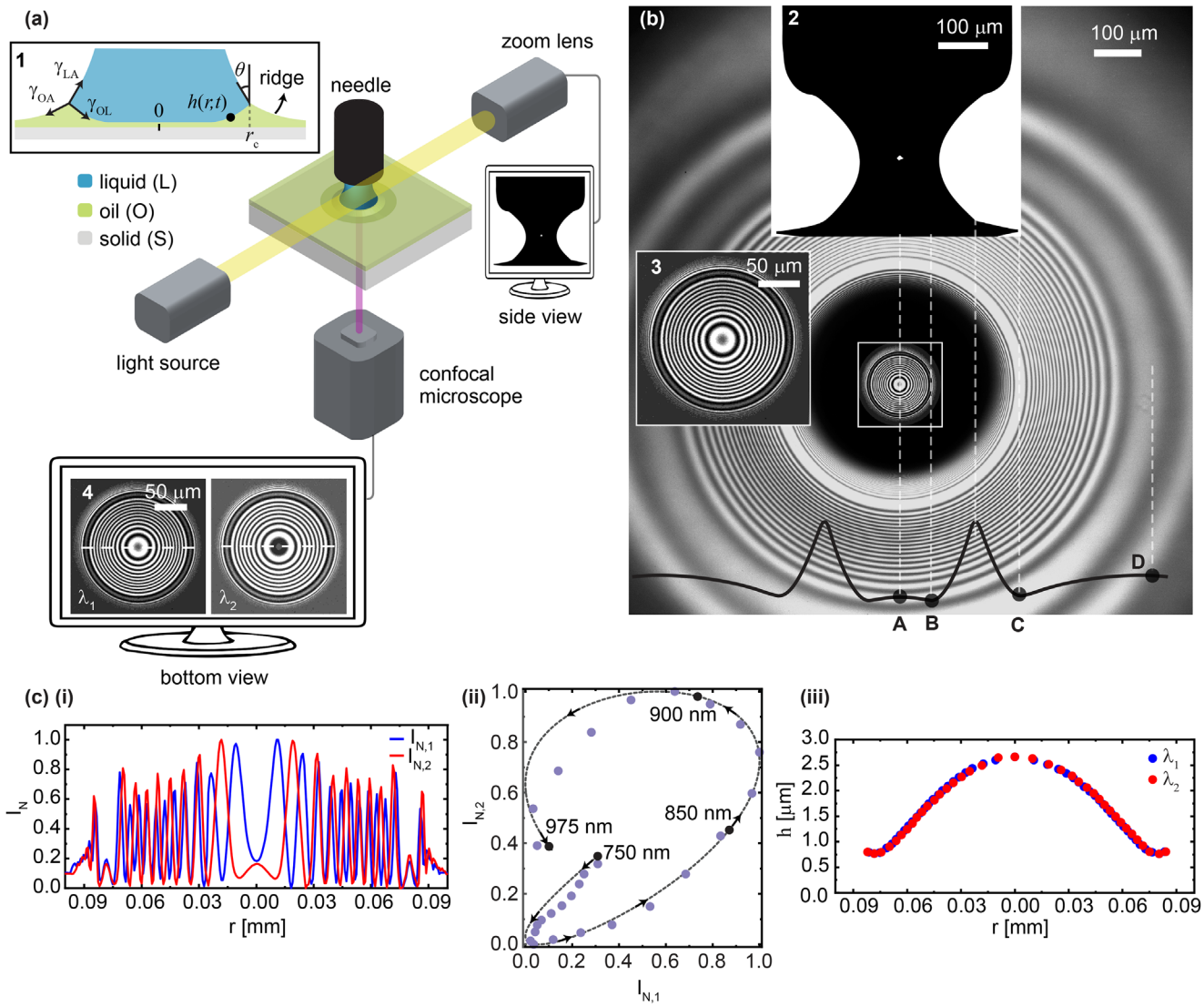

FIGURE 1 | Visualization of system. (a) Schematic of the experimental setup used to observe the system simultaneously from the side and bottom (Section S3 for more details). Inset 1 shows the schematic of the system.(b) Aligned side-view (inset 2) and bottom-view interferometry images of the system. The interference pattern (captured using a red laser with wavelength 638 nm) is due to the thin silicone oil film sandwiched between Krytox and glass. Brightness of the pattern beneath Krytox is enhanced for better visibility, and the magnified view is shown in inset 3. Spatial profile of the oil (not to scale) along the mid-section is displayed below, highlighting the film's local maxima and minima both beneath and beyond the liquid. The features are defined as A-center, B-edge, C-neck, and D-bump. (c) Methodology to determine the lubricant film profile using DW-RICM technique (Experimental section for more details). Briefly, the two normalized intensity profiles are analyzed, as shown in (i). Next, the intensity pairs near the edge are mapped onto the theoretical Lissajous curve to determine the thickness near the edge, as depicted in (ii). The thickness is then adjusted and finally the complete lubricant profile is reconstructed, as shown in (iii).

$r_c \sim 150\,\mu$m. In experiments with thinner films ($h_0 \sim 1\,\mu$m), we did not observe lift-off, whereas in experiments with thicker films ($h_0 \sim 6\,\mu$m), we consistently observed lift-off. Additionally, we found that for a fixed initial thickness, the lift-off time decreases with a decrease in the radius of three-phase contact line.

In addition to the faster drainage rate for the case of $h_{0,2}$, we also noted a significant increase in the size of wetting ridge, which led to a decrease in the values of r_c (from about 155 to 141 μm) and ΔP_{liq} (from about 44 to 36 Nm^{-2}) over time. For the case of $h_{0,1}$, however, we did not observe a significant change in the values of r_c (~153 μm) and ΔP_{liq} (~45 Nm^{-2}). Therefore, the experimental observations collectively indicate that thin-film dynamics beneath sessile liquids evolve through multiple stages, are strongly influenced by the initial film thickness and contact line radius, and can lead to liquid lift-off in specific cases.

To unveil the lubricant dynamics, we numerically solved the thin-film equation (Experimental Section and Section S9) [32–35]

$$\frac{\partial h}{\partial t} = \frac{1}{3r\mu}\frac{\partial}{\partial r}\left(rh^3\frac{\partial P_{\text{total}}}{\partial r}\right), \tag{1}$$

where μ is the viscosity of oil and P_{total} is the total pressure in the oil film. We denote the dimensionless forms of h, r, and t as $H(=h/h_0)$, $R(=r/r_c)$, and $T(=t/t_c)$, respectively, where

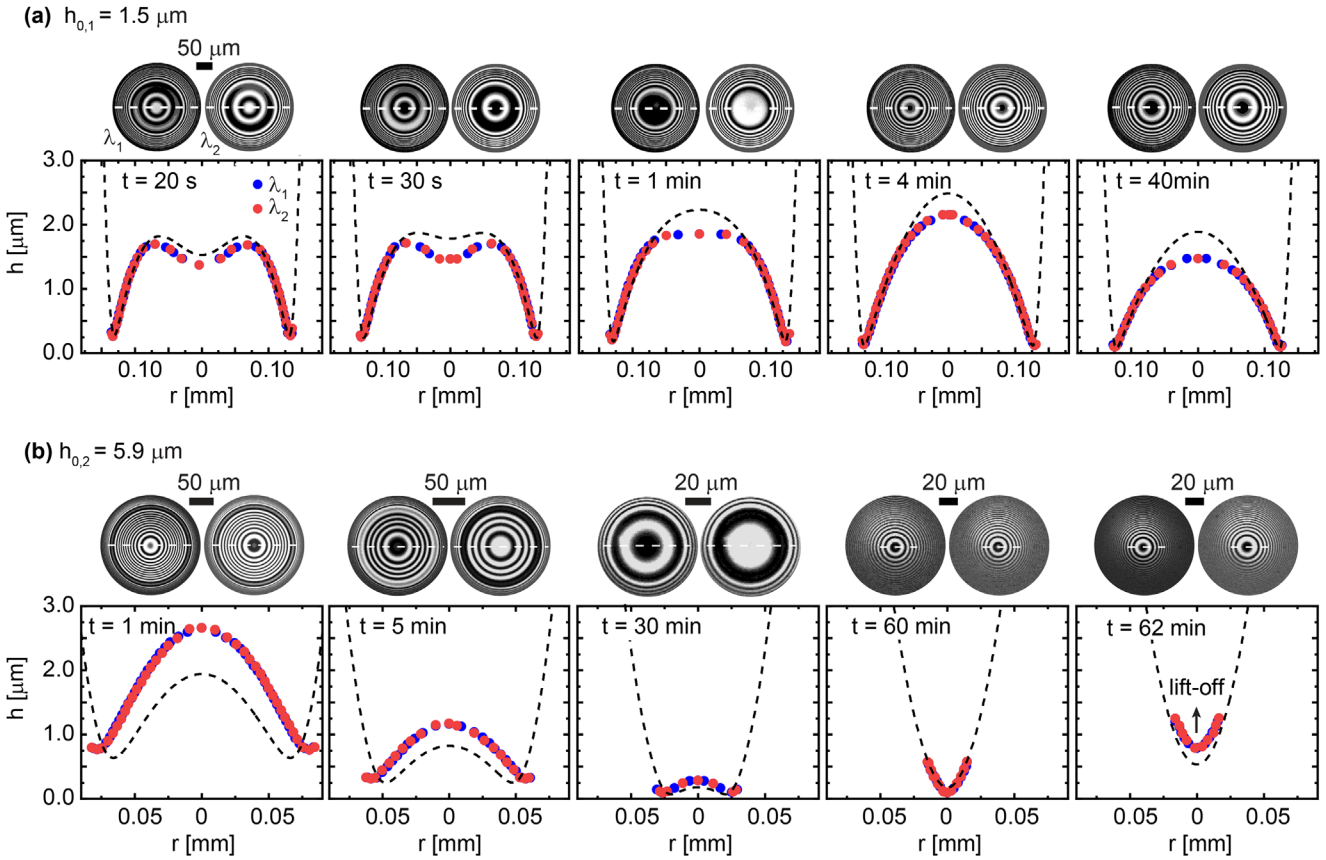

FIGURE 2 | Spatial evolution of lubricant film beneath sessile liquid. Interferometric images captured over time for a silicone oil film beneath sessile Krytox with initial film thicknesses (a) $h_{0,1} = 1.5\,\mu m$ and (b) $h_{0,2} = 5.9\,\mu m$ with corresponding determined profile along the midsection (depicted by white dashed lines) displayed in the bottom panels. The images are captured simultaneously using a blue ($\lambda_1 = 488$ nm) and a red laser ($\lambda_2 = 638$ nm), and the profiles are reconstructed from the intensity information. Blue and red filled circles correspond to the film height determined using blue and red lasers, respectively. The black dashed lines represent the numerical solutions. Film profile for the case of $h_{0,1}$ transitions from a wimple to a dimple, while no such transition is observed for the case of $h_{0,2}$. Instead, the edges merge and lead to liquid lift-off for the latter.

$t_c(= 3\mu r_c^4/\gamma_{OA}h_0^3)$ is the characteristic time scale. Note that this is an axisymmetric version of the model by Dai and Vella [28]. It is found that the lubricant dynamics in the early-intermediate times (defined as the interval in which most experiments are conducted) can be classified into three distinct stages based upon the local extrema of the center height evolution (Figure 3 and Movies S3 and S4).

Dynamics in stage-I. In the initial stage, I, the formation of a large negative Laplace pressure wetting ridge around $r = r_c$ causes the oil to rapidly flow from the surrounding area toward the wetting ridge, resulting in a fast decrease in the height at the endpoints of the wetting ridge (Figure 3a). The edge height falls faster than the neck height, as the oil beneath the liquid is driven by an extra pressure exerted by the liquid. The rapid decrease causes a non-uniform flow rate, which results in undulations beneath and beyond the liquid. The beneath undulations quickly smooth out to form a wimple profile, and the oil continues to flow toward the wetting ridge from both beneath and beyond the liquid. As time progresses, the maxima in the wimple propagate toward the center, resulting in a transition from wimple to dimple. This results in the rise of oil thickness at the center with the maximum thickness $h_{max,1}$ even exceeding h_0, which is also consistent with our experimental observation for the case of $h_{0,1}$. Numerically, we found that $h_{max,1}$ depends upon the oil volume present beneath the liquid during the merging of the maxima (Section S10).

Dynamics in stage-II. After the center reaches a maximum thickness, the dynamics enter stage-II, where the height at the center starts decreasing. The result is similar to the film drainage when a bubble or a liquid is pushed against a flat wall in another ambient liquid medium [35, 36]. During this period, the wetting ridge continues to grow, with the positions of the edge and the neck propagating toward and away from the center, respectively, while the height at the center and at the edge continues to decrease. Since the global minimum of the film is at the edge, it is the edge that reaches the van der Waals range ($h \sim 100$ nm) the quickest. Here, the stability of the film, and hence the minimum value h_{min}, depends upon the nature of the disjoining pressure. If the disjoining pressure is repulsive, it balances the Laplace pressure of the liquid, leading to $h_{min} \sim (A_{LOS}\, r_c/\gamma_{LA})^{1/3}$ and the oil beneath liquid continues to drain until the thickness at the center reaches the thickness at the edge [28, 29]. Here, A_{LOS} is the Hamaker constant representing the interaction of liquid and solid phases across the oil phase. Substituting typical values,

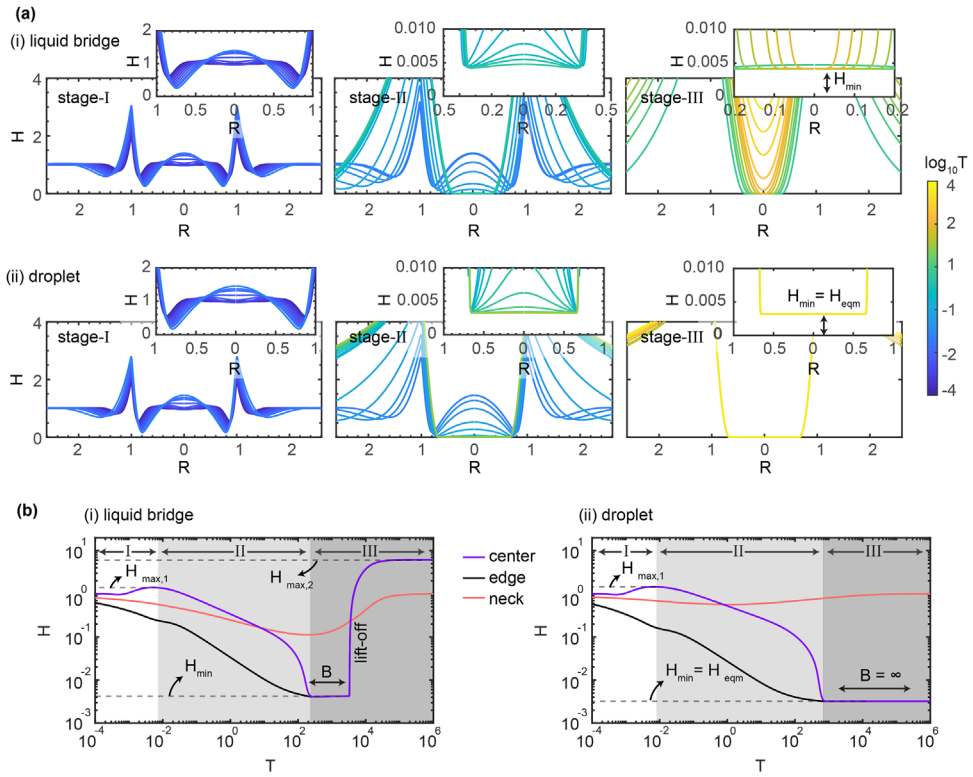

FIGURE 3 | Lubricant film dynamics: numerical solutions. (a) Spatial variation of dimensionless film height H with dimensionless position R upon contact with (i) a liquid bridge and (ii) a sessile droplet. The liquid is present in the region $0 \leq R \leq 1$. The change in dimensionless time T is depicted with different colors, with each color representing a different time as indicated by the colorbar on the right. The corresponding magnified view of the film profile beneath the liquid is displayed in the top panels. (b) Temporal variation of H at center, edge, and neck with dimensionless time T. Lubricant dynamics progress through three stages: I, II, and III. The thickness at the center reaches a maximum value $H_{\max,1}$ in stage-I and decreases to a minimum thickness $H_{\min}$ within the van der Waals range in stage-II. Dynamics in stage-III are different for the case of a liquid bridge and a sessile droplet. For the liquid bridge, depending on the system parameters, the merging of edges may occur in stage-III, resulting in either $H_{\min} = H_{\text{eqm}}$ if the edges do not merge, or $H_{\min} < H_{\text{eqm}}$ if they do. If the edges merge, the height at the center increases after a dimensionless waiting period B, leading to the liquid lift-off. Thus, B ranges from 0 to ∞. For the case of a sessile droplet, however, the edges do not merge, resulting in $H_{\min}$ becoming the equilibrium thickness H_{eqm}. The considered slippery system is Krytox, silicone oil, and glass as liquid, lubricant, and solid, respectively, with parameters $r_c = 248\mu\text{m}$, $\theta = 46°$, $h_0 = 6\mu\text{m}$, and $\Delta P_{\text{liq}} = 40$ and $95\ \text{Nm}^{-2}$ for the liquid bridge and the droplet, respectively.

$h_{\min}$ calculates to the order of tens of nanometers. This explains the experimental observation of the minimum height of about 22 nm located at the edge for the case of $h_{0,2}$ and also aligns with the previous study [29]. If the disjoining pressure is, however, attractive, the oil film ruptures at the edge and results in $h_{\min} \sim 0$ nm. Thus, for systems with unstable thin films beneath sessile liquids, the hole rupture should occur at the edge, which we also observed experimentally on non-modified glass substrates with Krytox and water as the test liquids (Figure S3 and Movie S5).

Dynamics in stage-III. Subsequent to stage-II, the film dynamics for slippery systems progress to the final stage, stage-III. In this stage, the lubricant dynamics depend upon the equilibrium shape of the oil-liquid interface and differ significantly for liquids with different Laplace pressures. For the case of large Laplace pressure liquid bridges and sessile droplets, the inward propagation of the edge stops and leads to the minimum thickness becoming the equilibrium thickness, i.e., $h_{\min} = h_{\text{eqm}}$. Conversely, for the case of low Laplace pressure liquid bridges, the edge continues to propagate inward and eventually merges after a time period b. Consistent with the experiments, our numerical results show that b decreases with increasing h_0 and/or decreasing r_c (Section S10). Physically, this behavior can be understood by considering how the wetting ridge closes at the center: a thicker lubricant layer supplies more volume for the ridge to grow and merge beneath the liquid, while a smaller contact line radius shortens the radial distance the ridge must traverse inward. The merging of edges results in the formation of a concave curvature of the oil-liquid interface (as seen from the oil phase), creating a pressure difference that drives the oil back toward the center. This leads to the lift-off of liquid from the slippery surface, explaining the experimental observation for the case of $h_{0,2}$. As the height at the center continues to rise, the system gradually approaches equilibrium. Interestingly, this phenomenon resembles the capillary rise of liquids in thin capillary tubes [4, 37].

The dashed lines in Figure 2 and Figure 4a,b show the numerical solutions for the experimental cases $h_{0,1}$ and $h_{0,2}$ (see Experimental Section for details), which are in excellent agreement with the experimental observations. For the case of $h_{0,1}$, numerical solutions predict the transition from stage-I to II at about 4 min and from stage-II to III at about 10^4 min. For the case of $h_{0,2}$, the corresponding transitions are predicted at 0.02 min and 58 min, respectively. Thus, the time scales involved in

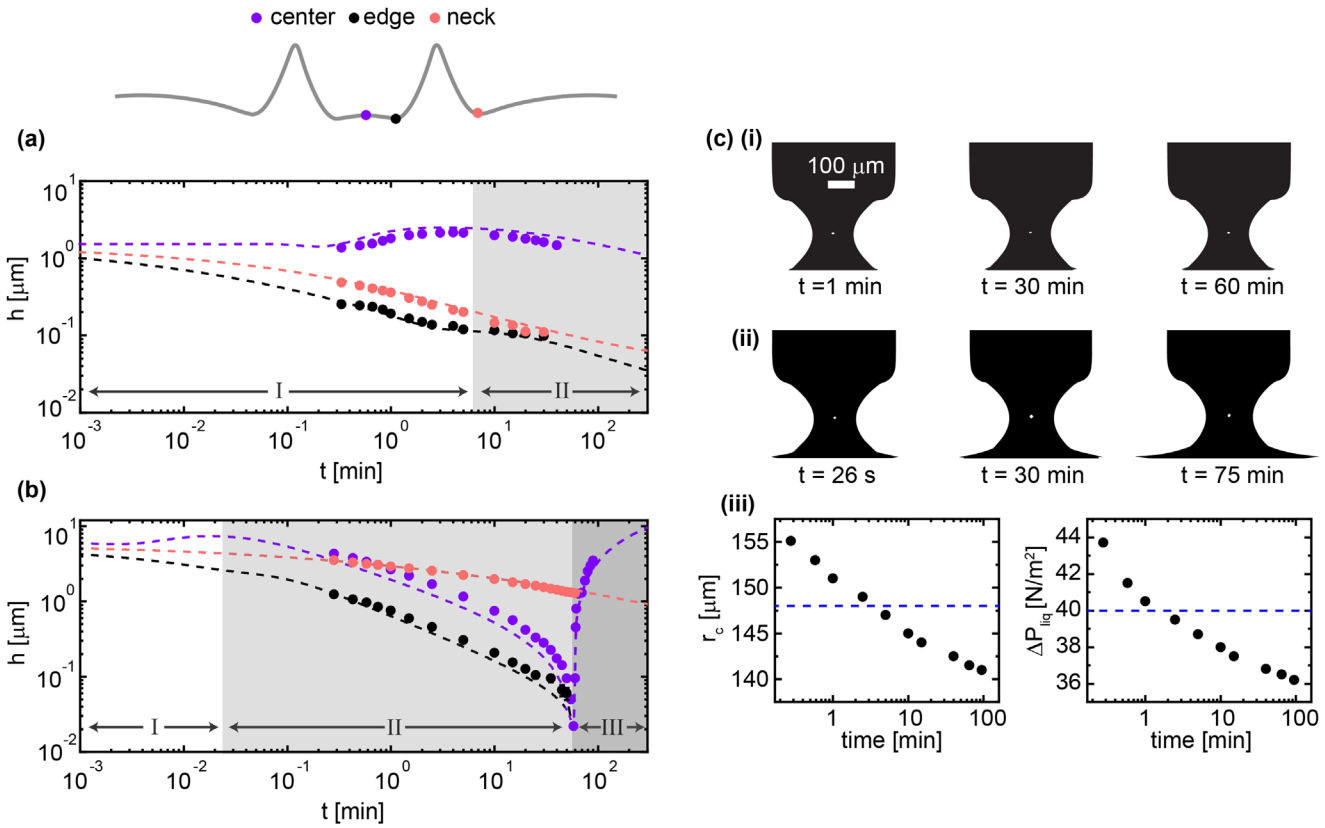

FIGURE 4 | Temporal evolution of lubricant film beneath sessile liquid bridge. Variation of film height h at features: center, edge, and neck with time t beneath sessile Krytox on a silicone oil-coated glass with initial film thickness (a) $h_{0,1} = 1.5\,\mu$m and (b) $h_{0,2} = 5.9\,\mu$m. The first two stages of the dynamics are observed for $h_{0,1}$, while the last two stages are observed for $h_{0,2}$. It takes about 4 min for the center to reach a maximum value of about 2.1μm for the case of $h_{0,1}$ and about 58 min to reach a minimum value of about 22 nm for the case of $h_{0,2}$. The experimental observations for the features are represented by filled circles, and the corresponding numerical solutions are shown by dashed lines, with the same color as the feature. (c) Variation in the Liquid's Laplace pressure and radius of the three-phase contact line in experiments. (i) and (ii) show the experimental side-view images captured at different times for the cases $h_{0,1}$ and $h_{0,2}$, respectively. Due to faster dynamics for thicker films, the wetting ridge grows significantly faster and thus leads to a significant variation in ΔP_{liq} and r_c, as shown in the semi-log plot in (iii). The blue horizontal dashed line corresponds to the average value ($r_c = 148\,\mu$m and $\Delta P_{\text{liq}} = 40\,\text{Nm}^{-2}$) used in the numerical computations.

stages-I and III are significantly different and make it experimentally challenging to capture all the three stages for a single system within a reasonable time frame. This is why we could not observe the height at the center reaching the van der Waals range (a feature of stage-III) for the case of $h_{0,1}$ and the formation of a wimple in the thin film (a feature of stage-I) for the case of $h_{0,2}$. The two thicknesses allowed us to partially access the three stages, with the thinner one allowing us to access the first two stages and the thicker one allowing us to access the last two stages. Another alternative would be to vary the radius of three-phase contact line, while keeping the initial thickness fixed. This also indicates that the lubricant dynamics and, consequently, the lubricant depletion can be suppressed by employing slippery systems with thinner films and foreign liquid droplets with larger volumes (Section S11).

2.2 | Dynamics Beyond Sessile Liquids

Along with the thin-film dynamics beneath sessile liquids, we also analyzed the dynamics of thin-film close to the bump. As shown in Figure 5, we found that throughout the three stages, the bump propagates outward according to the scaling law, $R_{\text{bump}} - R_{\text{neck}} \sim T^{1/4}$, with a prefactor of about 3.2, without significant variation in the film height at the bump h_{bump}. Here, R_{bump} and R_{neck} are the dimensionless positions of the bump and neck, respectively. A similar scaling law has also been reported previously for two-dimensional slippery systems and for the capillary-driven flow of thin viscous films [28, 38–40]. Figure 5b,c illustrates the observed behavior found from experiments and numerical solutions (dashed lines) for the cases $h_{0,1}$ and $h_{0,2}$ discussed previously, along with a new case $h_{0,3}$. For the case $h_{0,3}$, the system parameters were $\Delta P_{\text{liq}} \sim 42\,\text{Nm}^{-2}$, $r_c \sim 153\,\mu$m, and initial film thickness $h_{0,3} = 3.0\,\mu$m. We also numerically found the same scaling law for the case of sessile droplets, demonstrating the universality of the scaling law for sessile liquids.

To derive the scaling law, we refer to the approach adopted by Gonzalez et al. [40]. First, we consider the dominant terms contributing in the region close to the bump in Equation (1) to obtain

$$\frac{\partial h}{\partial t} = \frac{-\gamma_{\text{OA}}}{3r\mu}\frac{\partial}{\partial r}\left(rh^3\frac{\partial}{\partial r}\left(h_{rr} + \frac{h_r}{r}\right)\right). \tag{2}$$

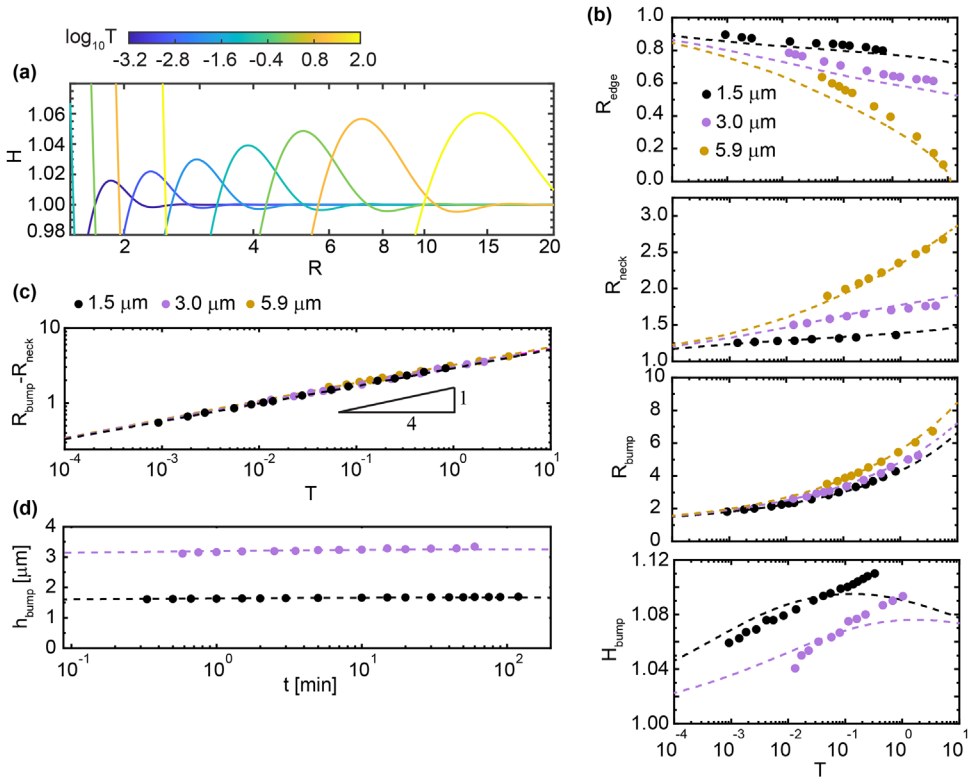

FIGURE 5 | Evolution of lubricant film close to bump. (a) Numerical solution for the evolution of the dimensionless film profile close to the bump. The colorbar corresponds to the dimensionless time T. (b) Change in dimensionless position and height over time for different h_0 (1.5, 3.0, and 5.9 μm). The dimensionless positions of the edge, neck, and bump are represented by R_{edge}, R_{neck}, and R_{bump}, respectively, while the dimensionless height of the bump is represented by H_{bump}. (c) Change in the dimensionless position of the bump relative to the neck $R_{bump} - R_{neck}$ as a function of T. The rescaled bump position follows power-law, $R_{bump} - R_{neck} \sim T^{1/4}$. (d) Variation in height at the bump h_{bump} with time t. The filled circles correspond to the experiments and the dashed lines (with the same color as the corresponding experiment) represent the numerical predictions. For (b)-(d), the filled circles correspond to the experimental observations, while the dashed lines (same color as the corresponding experiment) represent numerical solutions.

Next, since the bump propagates with nearly a constant height, we write $h = h_{bump} + \epsilon$ where $\epsilon \ll h_{bump}$. Finally, we approximate the scaling of $\nabla \sim 1/(r_{bump} - r_{neck})$ and substitute the physical quantities in their dimensionless form to obtain the observed scaling law.

2.3 | Configuration at Equilibrium

To investigate the effect of Laplace pressure of the liquid on the equilibrium configuration, we employed Surface Evolver (Experimental Section and Section S12 for more details) [41–44]. We varied the needle height relative to the surface z_n for the case of liquid bridges and the volume of liquid V_{liq} for the case of droplets. We found results similar to those predicted by our theoretical model for thin-film dynamics. For the case of a liquid bridge, we found that the merging of edges occurs for liquids with very low Laplace pressure. Figure 6a(i) illustrates one such example for Krytox, silicone oil, and glass system. With fixed values of $V_{liq} = 1\mu l$ and needle radius $r_n = 550\,\mu m$, lift-off occurred when ΔP_{liq} was reduced down to 13 Nm^{-2} for $z_n > 700\,\mu m$. A similar behavior was observed upon varying r_n with fixed z_n (Figure S9). For the case of a sessile droplet, however, we did not observe the merging of edge at any value of Laplace pressure. Instead, the distance from edge to the center increased with a decrease in Laplace pressure (Figure 6a(ii)). Experimentally, to observe near-equilibrium state of the thin film beneath sessile droplets, we captured the lubricant films beneath Krytox droplets on the lubricated surface after they had reached near equilibrium overnight. As shown in Figure 6b, we found absence of interference fringes beneath the droplet indicating that the film height at the center indeed approaches that at the edge, consistent with our numerical results for stage-III.

Analytically, the non-occurrence of lift-off for the sessile droplets can be understood by considering the possibility of merging of the edges. Let ϕ_1 and ϕ_2 be the angles that the interfacial tensions γ_{OL} and γ_{OA}, respectively, make with the vertical. If the edges were to merge, the oil-droplet interface would follow a spherical cap profile (neglecting hydrostatic pressure) with a Laplace pressure of $2\gamma_{OL}\cos\phi_1/r_c$. With $P_{oil} = P_{atm}$, the Laplace pressure of the droplet-air interface, $2\gamma_{LA}\cos\theta/r_c$, would need to be equal to $2\gamma_{OL}\cos\phi_1/r_c$. The balance of vertical forces at the three-phase contact line, $\gamma_{LA}\cos\theta = \gamma_{OL}\cos\phi_1 + \gamma_{OA}\cos\phi_2$ would then require $\phi_2 = 90°$, which is, in general, implausible. Therefore, for the case of sessile liquid droplets, the edges do not merge, and droplet lift-off does not occur. This is in contrast to liquid bridges, for which there is no such restriction on Laplace pressure, and therefore, lift-off occurs once $\Delta P_{liq} \sim 2\gamma_{OL}\cos\phi_1/r_c$.

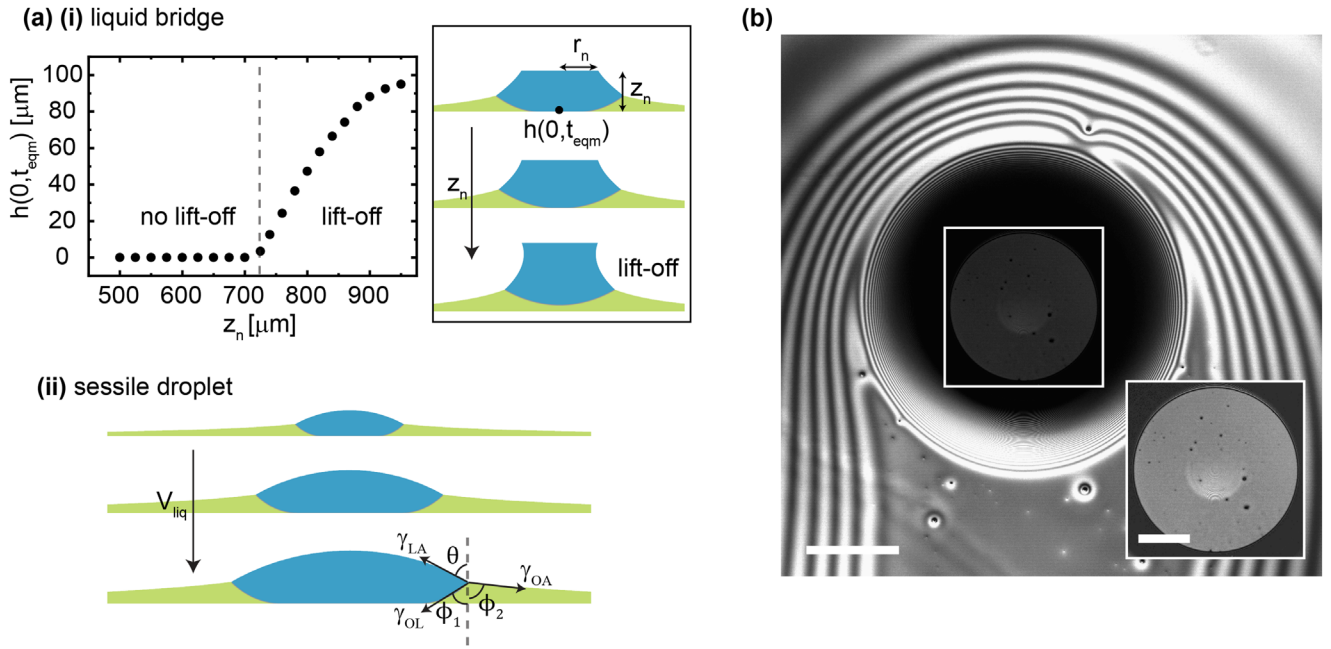

FIGURE 6 | Equilibrium configuration of system. (a)(i) Variation of equilibrium height at the center $h(0, t_{eqm})$ as a function of needle height z_n with fixed needle radius $r_n = 550\,\mu m$ for Krytox volume $V_{liq} = 1\mu l$. The liquid lift-off occurs for $z_n > 700\,\mu m$. The equilibrium configurations for $z_n = 600, 700$, and $1000\ \mu m$ arranged from top to bottom are displayed in the right panel. Similar behavior for lift-off is also observed with variation in r_n (Figure S9). (ii) Equilibrium configurations of the system upon contact with a sessile Krytox droplet with $V_{liq} = 10$, 50, and 100 nl (arranged from top to bottom) on a silicone oil-coated glass. For the case of a liquid bridge, the edges merge at low liquid pressure, whereas for a sessile droplet, the edges separate further as the pressure decreases. The configurations are numerically computed using Surface Evolver software (see Section S12 for details). (b) Long-time observation of film upon droplet contact. Bottom-view interferometry image captured after the Krytox droplet (without a supporting needle) is left overnight on a silicone oil-coated glass surface ($h_0 = 1.5\mu m$). Scale bar represents $200\,\mu m$. The magnified view beneath Krytox is shown (with enhanced brightness) in the bottom right corner, with a $100\,\mu m$ scale bar. The indistinct fringes visible at the droplet center arise from the curvature of the droplet-air interface.

3 | Conclusion

In summary, by using experiments, numerical modeling, and analytical calculations, we have provided a detailed understanding of the thin-film lubricant dynamics upon non-evaporating and immiscible positive Laplace pressure sessile liquids contact on slippery surfaces. We comprehensively investigated the dynamics associated with positive Laplace pressure liquid bridges and, owing to experimental limitations, provided theoretical insights into thin-film dynamics upon contact with sessile droplets, as well as into the equilibrium configurations of thin lubricant films upon contact with sessile liquids. We found that beneath sessile liquids, the lubricant films undergo three distinct stages of dynamics, while beyond liquids, the propagating bump follows a well-defined $T^{1/4}$ scaling law relative to the neck. The initial and late stage dynamics for the beneath films occur on very different timescales, making it experimentally challenging to access all three stages using a single system. To address this, we performed different sets of experiments with varying initial film thicknesses while keeping other parameters constant. While the first two stages of film dynamics are similar for sessile droplets and liquid bridges, the third stage can differ. For high Laplace pressure liquid bridges and droplets, the underlying film reaches an equilibrium thickness in the van der Waals interaction range. In contrast, for low Laplace pressure liquid bridges, the inner lubricant edges merge and the resulting pressure difference drives the lubricant back toward the center, leading to partial liquid lift-off. This phenomenon is notably similar to the capillary rise of liquids in thin tubes. Using Surface Evolver simulations, we further found that the equilibrium lift height can be tuned by adjusting the needle's height and width. Thus, beyond merely immobilizing the top liquid, the needle modifies the Laplace pressure of the liquid bridge, thereby influencing the film dynamics and dictating the lift-off and no-lift states of the system.

Prior knowledge of the lubricating film configuration upon liquid contact, as reported in this work, offers several potential advantages. First, it enables estimation of the total lubricant loss during droplet motion. As described by Kreder et al., the total amount of lubricant lost depends on two contributions: (i) the initial wetting ridge formed at droplet contact, and (ii) the additional ridge volume accumulated during droplet motion [26]. While the latter contribution was quantified, the initial ridge volume upon droplet contact remained unresolved. Our model provides first principle-based calculations of this initial ridge volume and therefore, when combined with the results of Kreder et al., offers a more complete framework for estimating total lubricant loss under droplet motion. Next, droplet coalescence, governed by the interaction of neighboring ridges, could also be examined using our model. For example, as shown in Section S11, larger initial film thicknesses enhance ridge growth and therefore are more likely to promote coalescence. However, future studies

are needed for a more quantitative understanding. Finally, in condensation-based heat exchangers, where heat is transferred through the sandwiched lubricant layer, the film thickness must directly influence the thermal resistance and thus the rate of heat transfer, as suggested by Fourier's law [45]. Our framework, therefore, may provide a means to estimate how evolving film thickness affects condensation performance. These examples illustrate how the present study may inform future investigations of technologically relevant processes.

In addition to slippery systems, our study also provides insights into systems with unstable thin films beneath sessile liquids. We found that the films beneath sessile liquids consistently rupture from the edge. This knowledge may offer a means to control the dewetted lubricant morphology and, consequently, the surface patterning. It also indicates that the surface fouling for such systems will initiate from the edge, which may offer a route to mitigate the fouling of lubricated surfaces.

While the film dynamics, both beneath and beyond sessile liquids, are in excellent agreement with our numerical calculations, it is important to note that our study addresses film dynamics for non-evaporating systems on texture-free solid surfaces. For lubricant-infused slippery systems involving evaporating water droplets, our results may serve as a reference for decoupling and analyzing the separate effects of evaporation and lubricant confinement. It remains an open research problem as to how the interplay between decreasing r_c, increasing ΔP_{liq}, and varying θ over time for the evaporating droplet, alongside the additional capillary pressure of the confined lubricant, influences film dynamics in such systems. Furthermore, while we have used a perfluorinated oil as the test liquid, which has a low surface tension and a specific wetting behavior, we expect the same qualitative behavior (with different quantitative characteristics) of thin-film dynamics for non-evaporating systems on texture-free solid surfaces with different disjoining pressures and interfacial tension ratios, as long as they satisfy the thin-film stability criteria (Section S13). Altogether, the present study reveals interfacial behaviors that were previously difficult to access and observe, offering a more comprehensive understanding of the mechanisms governing lubricant dynamics with potential in several applications.

4 | Experimental Section

4.1 | Sample Preparation

We used glass coverslips as the solid substrates. Silicone oil (Gelest) with kinematic viscosity 1000×10^{-6} m^2 s^{-1}, density 971 Kg m^{-3} and surface tension 21 mN m^{-1}, was used as the lubricant. For the non-evaporating liquid with a high refractive index contrast with silicone oil, we chose Krytox VPF-1506 (Chemours) with kinematic viscosity 60×10^{-6} m^2 s^{-1}, density 1880 Kg m^{-3}, and surface tension 17.0 ± 0.5 mN m^{-1}. The interfacial tension value for the oil-liquid interface ($\gamma_{OL} = 8.0 \pm 0.8$ mN m^{-1}) was determined using the pendant drop method, conducted with a contact angle goniometer (DataPhysics, OCA 35) [46].

For the system of Krytox, silicone oil, and glass, while $A_{LOS} > 0$, the low contact angle of Krytox on glass results in $S_{OSL}(= \gamma_{LS} - \gamma_{OL} - \gamma_{OS}) < 0$ (Section S5). However, for a thin film of lubricant to be stable, the system must satisfy $A_{LOS} > 0$ and $S_{OSL} > 0$ [29]. Thus, to decrease the wettability of Krytox on glass, the substrates were chemically modified by grafting polydimethylsiloxane (PDMS) chains. The procedure is as follows [47–49]. First, the substrates were exposed to oxygen plasma (Harrick Plasma) for 15 min, then spin coated with silicone oil, and subsequently heated at 150°C for 10 h. Afterward, the non-grafted oil was removed by first rinsing and then ultrasonicating the samples in toluene (99.5 %, Loba Chemie) for 10 min.

4.2 | Determining Thickness of Grafted Chains

We employed the X-Ray Reflectivity (XRR) technique (PANanalytical X'pert Pro, $\lambda = 1.54$ Å) to determine the thickness of the grafted PDMS chains. By analyzing the positions of the maxima and minima in the reflectivity data, we determined the approximate thickness of the chains to be about 7 nm. The details can be found in the Section S6.

4.3 | Determining Initial Film Thickness

Glass coverslips with a few µl oil droplets dispensed on top were spun at varying angular speeds to achieve different film thicknesses using a commercial spin coater (spinXG-P1, Apex). Specifically, the coverslips were spun at 4300 rpm for 100 s, 8100 rpm for 100 s, and 10 000 rpm for 240 s to achieve thicknesses of 5.9, 3.0, and 1.5 µm, respectively, with an uncertainty of ±0.1 µm. The thicknesses were measured using a custom-built thickness measurement setup employing an inverted microscope (IX-73, Olympus), a spectrometer (HR-4000, Ocean Optics), and a metal halide light source (U-HGLGPS, Olympus). A 4× magnification objective with a 0.1 numerical aperture (NA) was used to focus the light on the sample. See Section S2 for more details.

4.4 | Side-View Imaging

A halogen light source (Radical Scientific Equipments Pvt. Ltd.) and a zoom lens (Edmund Optics) were employed to observe the system from the side. The default height of the confocal sample stage, however, does not permit a side view. To address this, we designed a custom acrylic stage with a height of about 8 mm and a through hole of about 15 mm diameter. This elevated the sample, allowing the system to be viewed simultaneously from both the side and bottom.

4.5 | Bottom-View Imaging

The thin-film interference was observed using a confocal microscope (Leica Stellaris 5) in the reflection mode. Blue and red lasers with wavelengths $\lambda_1 = 488$ nm and $\lambda_2 = 638$ nm, respectively, were simultaneously incident at the sample, and the reflected light corresponding to the two lasers was collected by two separate detectors. The light was focused on the thin film from a 10× objective with 0.3 NA. The pinhole size was set to 2 airy units. The image was captured at a scan speed of 600 Hz with a pixel dwell time of about 0.425 µs. The resolution of the image was 2048×2048 pixels with a pixel size of 0.757 µm. The physical size

of the image was 1550 μm along both the horizontal and vertical directions. The laser intensities were adjusted such that both the inner ($r < r_c$) and outer interference fringes ($r > r_c$) were clearly visible simultaneously.

4.6 | Determining Laplace Pressure of Liquid

The Laplace pressure of the liquid was determined by employing Surface Evolver, a finite element software that computes the equilibrium liquid configuration subject to various constraints [41, 42]. From the known constraints and values of z_n, r_n, and r_c, the configuration and hence the Laplace pressure of the liquid bridge were calculated. The details can be found in the Section S8.

4.7 | Determining Dynamic Film Thickness

To determine the thin-film profile, we employed DW-RICM technique [29, 50–52]. First, the normalized intensity profiles, as shown in Figure 1c(i), are obtained across the region of interest (e.g., white horizontal dashed lines in inset 4). The intensity pairs near the edge are then mapped onto the theoretical Lissajous curve (see Section S4 for the equation) to determine the thickness near the edge, as depicted in Figure 1c(ii). For the example shown, the experimental normalized intensity pair (filled circles) follows the theoretical Lissajous curve (black dashed line) ranging from 750 to 975 nm (black dashed curve), implying the thickness near the edge is about 750 nm. The thickness is then adjusted by $\lambda/4n_{oil}$ based on the positions of adjacent maxima and minima. Here, n_{oil} is the refractive index of oil. Finally, the thickness at the center is determined again using the Lissajous curve. Thus, the complete lubricant profile is reconstructed using the two wavelengths, as shown in Figure 1c(iii).

4.8 | Solving Thin-Film Dynamics

We employed a two-dimensional axisymmetric model in the $r-z$ plane to theoretically analyze the dynamics of thin films both beneath and beyond the liquid. For slippery systems, the length scale along r is generally much larger than that along z, and the no-slip boundary condition is satisfied at the oil-solid interface. Thus, we employed the Stokes–Reynolds equation in cylindrical coordinates. The equation relates the rate of change of thickness $\partial h(r,t)/\partial t$ to P_{total} and μ of the oil film as [32–35]

$$\frac{\partial h}{\partial t} = \frac{\beta}{12r\mu}\frac{\partial}{\partial r}\left(rh^3\frac{\partial P_{total}}{\partial r}\right), \tag{3}$$

where the value of constant β depends upon the boundary condition at the oil-liquid interface. The value of $\beta = 4$, if a zero tangential stress boundary condition is satisfied at the oil-liquid interface, while $\beta = 1$ if no-slip or tangentially immobile boundary condition is satisfied at the interface. For the present case, the viscosity of liquid is about ten times smaller than that of the lubricant. Thus, we considered $\beta = 4$. Due to the presence of liquid in the region, $r \le r_c$, the total pressure within the oil film, relative to atmospheric pressure, differs across the regions $r < r_c$, $r = r_c$, and $r > r_c$ and can be expressed as

$$\begin{aligned} P_{total} = &\left[\Delta P_{liq} - \gamma_{OL}\left(h_{rr} + \frac{h_r}{r}\right) - \frac{A_{LOS}}{6\pi h^3}\right]U(r_c - r) \\ &\left[-\gamma_{OA}\left(h_{rr} + \frac{h_r}{r}\right) - \frac{A_{AOS}}{6\pi h^3}\right]U(r - r_c) \\ &- \gamma_{LA}\cos\theta\,\delta(r - r_c) + \rho g(h - z), \end{aligned} \tag{4}$$

where A_{AOS} is the non-retarded Hamaker constant corresponding to the interaction between the air and solid phase across the oil phase (Section S5). For the sessile droplets, $\Delta P_{liq} = 2\gamma_{LA}\cos\theta/r_c$, while for the liquid bridges, it needs to be determined from the side view. The coefficients U and δ are the unit step and delta functions, respectively, and θ is the angle that γ_{LA} makes with the vertical. We assumed small slopes in the oil film, $|h_r| \ll 1$ to approximate the mean curvature of the oil-liquid and oil-air interfaces. To numerically solve the Stokes–Reynolds equation, we non-dimensionalized h, r, and t using the characteristic scales for the early-intermediate times h_0, r_c, and t_c, respectively, and applied the following boundary conditions for $h(r,t)$ [28]:

$$h_r(0,t) = h_r(r_\infty,t) = h_{rrr}(0,t) = h_{rrr}(r_\infty,t) = 0, \tag{5}$$

where r_∞ is the position far from the liquid. The scales for early-intermediate time were particularly chosen because this time encompasses the conditions of most experimental observations. Using the central finite difference technique and method of lines, a set of ODEs was obtained for Equation (3), which was solved numerically using MATLAB's built-in solver ode15s. The connection of the inner and the outer menisci was achieved by using the smoothed form of delta and step functions similar to the method described by Dai and Vella [28]. The details can be found in the Section S9.

4.9 | Fitting Experimental Results With Numerical Predictions

To fit the experimental observations with numerical results, we considered the average values of r_c and ΔP_{liq} and varied the values of γ_{OL} within the uncertainty limits ($\gamma_{OL} = 8.0 \pm 0.8$ mN m^{-1}) and θ within the dynamic range ($\theta = 44° - 47°$). We found good quantitative agreement for $\gamma_{OL} = 8.7$ mN m^{-1} and $\theta = 46°$ and 47° for $h_0 = 5.9\,\mu$m and 1.5 μm, respectively. A more refined approach would be to dynamically update r_c, ΔP_{liq}, and θ over time, an aspect that future studies may address.

4.10 | Determining Equilibrium Configuration

The equilibrium configuration of the system was determined by employing Surface Evolver. We set the Laplace pressure of oil at $z = 0$ equal to zero and let the system evolve. For the liquid bridge, the upper vertices were constrained to lie on a circular boundary with a fixed radius r_n (Section S12). We did not consider intermolecular interactions, as they are expected to primarily govern the stability of thin films and the time required to reach equilibrium, rather than the equilibrium macroscopic profile [28].

Acknowledgments

We thank V. J. Yallapragada for fruitful discussions. The research work received funding support from DST under FIST (Project No. SR/FST/PS-II/2021/170) and AMT (Project No. DST/TDT/AM/2022/285) schemes, ANRF (Project No. CRG/2023/008576) under the CRG scheme and MoE (Project No. MoE-STARS/STARS-2/2023-0773) under the STARS scheme. S.G. acknowledges financial support from the Prime Minister's Research Fellows (PMRF) scheme of the Government of India.

Conflicts of Interest

The authors declare no conflicts of interest.

Data Availability Statement

The data that support the findings of this study are available from the corresponding author upon reasonable request.

References

1. W. Barthlott and C. Neinhuis, "Purity of the Sacred Lotus, or Escape from Contamination in Biological Surfaces," *Planta* 202 (1997): 1–8.

2. Y. Yan, N. Gao, and W. Barthlott, "Mimicking Natural Superhydrophobic Surfaces and Grasping the Wetting Process: A Review on Recent Progress in Preparing Superhydrophobic Surfaces," *Advances in Colloid and Interface Science* 169, no. 2 (2011): 80–105.

3. D. Quéré, "Non-Sticking Drops," *Reports on Progress in Physics* 68, no. 11 (2005): 2495.

4. P.-G. Gennes, F. Brochard-Wyart, and D. Quéré, *Capillarity and Wetting Phenomena: Drops, Bubbles, Pearls, Waves* (Springer, 2004).

5. A. Lafuma and D. Quéré, "Superhydrophobic States," *Nature Materials* 2, no. 7 (2003): 457–460.

6. C. Dorrer and J. Rühe, "Condensation and Wetting Transitions on Microstructured Ultrahydrophobic Surfaces," *Langmuir* 23, no. 7 (2007): 3820–3824.

7. G. B. Hwang, K. Page, A. Patir, S. P. Nair, E. Allan, and I. P. Parkin, "The Anti-Biofouling Properties of Superhydrophobic Surfaces Are Short-Lived," *ACS Nano* 12, no. 6 (2018): 6050–6058.

8. K. K. Varanasi, T. Deng, J. D. Smith, M. Hsu, and N. Bhate, "Frost Formation and Ice Adhesion on Superhydrophobic Surfaces," *Applied Physics Letters* 97, no. 23 (2010): 234102.

9. R. H. A. Ras and A. Marmur, *Non-Wettable Surfaces: Theory, Preparation, and Applications* (The Royal Society of Chemistry, 2016).

10. X. Zhou, P. Sudersan, D. Diaz, et al., "Chemically Robust Superhydrophobic Surfaces with a Self-Replenishing Nanoscale Liquid Coating," *Droplet* 3, no. 1 (2024): e103.

11. C. Yue, Q. Dai, X. Yang, C. Gachot, W. Huang, and X. Wang, "Controllable Self-Transport of Bouncing Droplets on Ultraslippery Surfaces with Wedge-Shaped Grooves," *Droplet* 3, no. 2 (2024): e118.

12. H. F. Bohn and W. Federle, "Insect Aquaplaning: Nepenthes Pitcher Plants Capture Prey with the Peristome, a Fully Wettable Water-Lubricated Anisotropic Surface," *Proceedings of the National Academy of Sciences of the United States of America* 101, no. 39 (2004): 14138–14143.

13. U. Bauer and W. Federle, "The Insect-Trapping Rim of Nepenthes Pitchers: Surface Structure and Function," *Plant Signaling and Behavior* 4, no. 11 (2009): 1019–1023.

14. C. Wang and Z. Guo, "A Comparison Between Superhydrophobic Surfaces (SHS) and Slippery Liquid-Infused Porous Surfaces (SLIPS) in Application," *Nanoscale* 12, no. 44 (2020): 22398–22424.

15. T.-S. Wong, S. H. Kang, S. K. Tang, et al., "Bioinspired Self-Repairing Slippery Surfaces with Pressure-Stable Omniphobicity," *Nature* 477, no. 7365 (2011): 443–447.

16. P. Kim, T.-S. Wong, J. Alvarenga, M. J. Kreder, W. E. Adorno-Martinez, and J. Aizenberg, "Liquid-Infused Nanostructured Surfaces with Extreme Anti-Ice and Anti-Frost Performance," *ACS Nano* 6, no. 8 (2012): 6569–6577.

17. M. J. Kreder, J. Alvarenga, P. Kim, and J. Aizenberg, "Design of Anti-Icing Surfaces: Smooth, Textured or Slippery?" *Nature Reviews Materials* 1 (2016): 15003.

18. X. Dai, N. Sun, S. O. Nielsen, et al., "Hydrophilic Directional Slippery Rough Surfaces for Water Harvesting," *Science Advances* 4, no. 3 (2018): eaaq0919.

19. S. Anand, A. T. Paxson, R. Dhiman, J. D. Smith, and K. K. Varanasi, "Enhanced Condensation on Lubricant-Impregnated Nanotextured Surfaces," *ACS Nano* 6, no. 11 (2012): 10122–10129.

20. A. K. Epstein, T.-S. Wong, R. A. Belisle, E. M. Boggs, and J. Aizenberg, "Liquid-Infused Structured Surfaces with Exceptional Anti-Biofouling Performance," *Proceedings of the National Academy of Sciences of the United States of America* 109, no. 33 (2012): 13182–13187.

21. J. D. Smith, R. Dhiman, S. Anand, E. Reza-Garduno, R. E. Cohen, G. H. McKinley, and K. K. Varanasi, "Droplet Mobility on Lubricant-Impregnated Surfaces," *Soft Matter* 9 (2013): 1772–1780.

22. A. Keiser, L. Keiser, C. Clanet, and D. Quéré, "Drop Friction on Liquid-Infused Materials," *Soft Matter* 13 (2017): 6981–6987.

23. J. B. Boreyko, G. Polizos, P. G. Datskos, S. A. Sarles, and C. P. Collier, "Air-Stable Droplet Interface Bilayers on Oil-Infused Surfaces," *Proceedings of the National Academy of Sciences of the United States of America* 111, no. 21 (2014): 7588–7593.

24. H. Xu, Y. Zhou, D. Daniel, J. Herzog, X. Wang, V. Sick, and S. Adera, "Droplet Attraction and Coalescence Mechanism on Textured Oil-Impregnated Surfaces," *Nature Communications* 14, no. 1 (2023): 4901.

25. P. Baumli, M. D'Acunzi, K. I. Hegner, et al., "The Challenge of Lubricant-Replenishment on Lubricant-Impregnated Surfaces," *Advances in Colloid and Interface Science* 287 (2021): 102329.

26. M. J. Kreder, D. Daniel, A. Tetreault, et al., "Film Dynamics and Lubricant Depletion by Droplets Moving on Lubricated Surfaces," *Physical Review X* 8 (2018): 031053.

27. J. S. Wexler, I. Jacobi, and H. A. Stone, "Shear-Driven Failure of Liquid-Infused Surfaces," *Physical Review Letters* 114 (2015): 168301.

28. Z. Dai and D. Vella, "Droplets on Lubricated Surfaces: The Slow Dynamics of Skirt Formation," *Physical Review Fluids* 7 (2022): 054003.

29. D. Daniel, J. V. Timonen, R. Li, S. J. Velling, and J. Aizenberg, "Oleoplaning Droplets on Lubricated Surfaces," *Nature Physics* 13, no. 10 (2017): 1020–1025.

30. A. Lafuma and D. Quéré, "Slippery Pre-Suffused Surfaces," *Europhysics Letters* 96, no. 5 (2011): 56001.

31. L. Y. Clasohm, J. N. Connor, O. I. Vinogradova, and R. G. Horn, "The Wimple: Rippled Deformation of a Fluid Drop Caused by Hydrodynamic and Surface Forces During Thin Film Drainage," *Langmuir* 21, no. 18 (2005): 8243–8249.

32. C.-Y. Lin and J. C. Slattery, "Thinning of a Liquid Film as a Small Drop or Bubble Approaches a Solid Plane," *AIChE Journal* 28 (1982): 147–156.

33. A. Nguyen and H. J. Schulze, *Colloidal Science of Flotation* (CRC Press, 2003).

34. L. G. Leal, *Advanced Transport Phenomena: Fluid Mechanics and Convective Transport Processes* (Cambridge University Press, 2007), vol. 7.

35. D. Y. C. Chan, E. Klaseboer, and R. Manica, "Film Drainage and Coalescence Between Deformable Drops and Bubbles," *Soft Matter* 7 (2011): 2235–2264.

36. R. Manica and D. Y. C. Chan, "Drainage of the Air-Water-Quartz Film: Experiments and Theory," *Physical Chemistry Chemical Physics* 13 (2011): 1434–1439.

37. J. Jurin, "An Account of Some Experiments Shown Before the Royal Society; with an Enquiry into the Cause of the Ascent and Suspension of Water in Capillary Tubes," *Philosophical Transactions of the Royal Society* 30, no. 355 (1718): 739–747, https://www.jstor.org/stable/103321.

38. J. D. McGraw, T. Salez, O. Bäumchen, E. Raphaël, and K. Dalnoki-Veress, "Self-Similarity and Energy Dissipation in Stepped Polymer Films," *Physical Review Letters* 109, no. 12 (2012): 128303.

39. Z. Zheng, M. A. Fontelos, S. Shin, et al., "Healing Capillary Films," *Journal of Fluid Mechanics* 838 (2018): 404–434.

40. D. Garcia-Gonzalez, M. A. Hack, M. Kappl, H.-J. Butt, and J. H. Snoeijer, "Drawing Liquid Bridges from a Thin Viscous Film," *Soft Matter* 19 (2023): 1241–1248.

41. K. A. Brakke, "The Surface Evolver," *Experimental Mathematics* 1, no. 2 (1992): 141–165.

42. K. A. Brakke, *Surface Evolver Manual* (Mathematics Department, Susquehanna University, Selinsgrove, PA, U.S.A, 1994).

43. C. Semprebon, G. McHale, and H. Kusumaatmaja, "Apparent Contact Angle and Contact Angle Hysteresis on Liquid Infused Surfaces," *Soft Matter* 13 (2017): 101–110.

44. S. Gupta, B. Bhatt, M. Sharma, and K. Khare, "Numerical and Experimental Investigation of Static Wetting Morphologies of Aqueous Drops on Lubricated Slippery Surfaces Using a Quasi-Static Approach," *Soft Matter* 19 (2023): 1164–1173.

45. F. P. Incropera, D. P. DeWitt, T. L. Bergman, et al., *Fundamentals of Heat and Mass Transfer* (New York John Wiley & Sons, Inc., 1990), vol. 1072.

46. C. E. Stauffer, "The Measurement of Surface Tension by the Pendant Drop Technique," *The Journal of Physical Chemistry A* 69, no. 6 (1965): 1933–1938.

47. J. W. Krumpfer and T. J. McCarthy, "Contact Angle Hysteresis: A Different View and a Trivial Recipe for Low Hysteresis Hydrophobic Surfaces," *Faraday Discussions* 146 (2010): 103–111.

48. J. W. Krumpfer and T. J. McCarthy, "Rediscovering Silicones: "Unreactive" Silicones React with Inorganic Surfaces," *Langmuir* 27, no. 18 (2011): 11514–11519.

49. L. Chen, S. Park, J. Yoo, et al., "One-Step Fabrication of Universal Slippery Lubricated Surfaces," *Advanced Materials Interfaces* 7, no. 18 (2020): 2000305.

50. A. Curtis, "The Mechanism of Adhesion of Cells to Glass: A Study by Interference Reflection Microscopy," *Journal of Cell Biology* 20, no. 2 (1964): 199–215.

51. J. Schilling, K. Sengupta, S. Goennenwein, A. R. Bausch, and E. Sackmann, "Absolute Interfacial Distance Measurements by Dual-Wavelength Reflection Interference Contrast Microscopy," *Physical Review E* 69 (2004): 021901.

52. L. Limozin and K. Sengupta, "Quantitative Reflection Interference Contrast Microscopy (RICM) in Soft Matter and Cell Adhesion," *ChemPhysChem* 10, no. 16 (2009): 2752–2768.

Supporting Information

Additional supporting information can be found online in the Supporting Information section.

Supporting File: 1 smll73895-sup-0001-SuppMat.pdf.

Supporting File: 2 smll73895-sup-0002-VideoS1.mp4.

Supporting File: 3 smll73895-sup-0003-VideoS2.mp4.

Supporting File: 4 smll73895-sup-0004-VideoS3.mp4.

Supporting File: 5 smll73895-sup-0005-VideoS4.mp4.

Supporting File: 6 smll73895-sup-0006-VideoS5.mp4.